

pubs.acs.org/journal/apchd5 Article

Optical Dipole Structure and Orientation of GaN Defect Single-Photon Emitters

Yifei Geng,* Debdeep Jena, Gregory D. Fuchs, Warren R. Zipfel, and Farhan Rana



Cite This: ACS Photonics 2023, 10, 3723–3729



Read Online

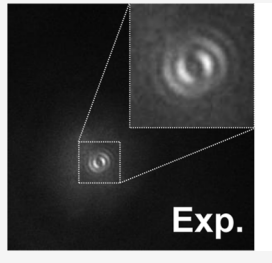
ACCESS I

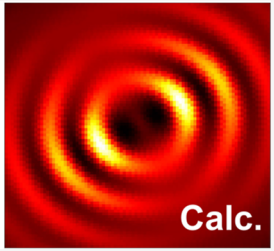
III Metrics & More

Article Recommendations

s Supporting Information

ABSTRACT: GaN has recently been shown to host bright, photostable, defect single-photon emitters in the 600–700 nm wavelength range that are promising for quantum applications. The nature and origin of these defect emitters remain elusive. In this work, we study the optical dipole structures and orientations of these defect emitters using the defocused imaging technique. In this technique, the far-field radiation pattern of an emitter in the Fourier plane is imaged to obtain information about the structure of the optical dipole moment and its orientation in 3D. Our experimental results, backed by numerical simulations, show that these defect emitters in GaN exhibit a single dipole moment that is oriented almost perpendicular to the





wurtzite crystal *c*-axis. Data collected from many different emitters show that the angular orientation of the dipole moment in the plane perpendicular to the *c*-axis exhibits a distribution that shows peaks centered at the angles corresponding to the nearest Ga–N bonds and also at the angles corresponding to the nearest Ga–Ga (or N–N) directions. Moreover, the in-plane angular distribution shows little difference among defect emitters with different emission wavelengths in the 600–700 nm range. Our work sheds light on the nature and origin of these GaN defect emitters.

KEYWORDS: GaN defect, Single photon emitter, Defocused imaging, Optical dipole, Solid immersion lens

INTRODUCTION

Single-photon emitters (SPEs) play an important role in quantum computing and quantum communication technologies. SPEs with high brightness, high photon indistinguishability, a narrow emission spectrum, small blinking effects, and integration compatibility with technologically important material platforms are desired for quantum applications. A family of defect-based SPEs in GaN in the 600-700 nm wavelength range has been reported to exhibit high brightness and sharp zero phonon lines (ZPL) even at room temperature, 2,3 making these defects very promising for single-photon applications. Recently, optically detected magnetic resonance was also reported in these GaN defect states.⁴ However, very little is known thus far about the origin of these defects. Point defects in the form of substitutional impurity atoms, or impurityvacancy complexes, and defect states near dislocations or stacking faults^{2,3} have been proposed as candidates for these SPEs in the literature. The identification of the nature and origin of these defect SPEs is an important first step in harnessing their potential for applications.

A topic of special interest in this context is the determination of the spatial orientation of the defect's optical dipole moment. The spatial orientation of the dipole moment, as shown in Figure 1a, is specified by the angle θ_o from the z-axis (henceforth assumed to be parallel to the c-axis of the wurtzite crystal) and the angle φ_o in the plane perpendicular to the c-axis. On one hand, the dipole orientation strongly affects the

design and efficiency of optical structures (gratings, microcavities, waveguides, etc.) needed to couple photons out of the defect, and on the other hand, the dipole orientation can say a lot about the nature of the defect and its environment. A few different experimental techniques have been demonstrated to determine the 3D orientation of the optical dipole moment of an emitter.⁶⁻⁸ The simplest ones among these are based on light collection from the dipole and either record the image at the back focal plane of the objective⁹ or record the emission pattern with an objective that is defocused with respect to the dipole 10-13 and then use analytical models or numerical computations to determine the orientation of the dipole from the recorded image data. The accuracy of both these techniques is generally around ±15° but can be as good as $\pm 5^{\circ}$ depending on the photon collection efficiency of the measurement setup and the available signal-to-noise ratio. The defocused imaging technique has been previously used to determine the optical dipole orientation in colloidal quantum dots^{14–16} and dye molecules.^{17,18}

Received: June 30, 2023 Published: October 5, 2023





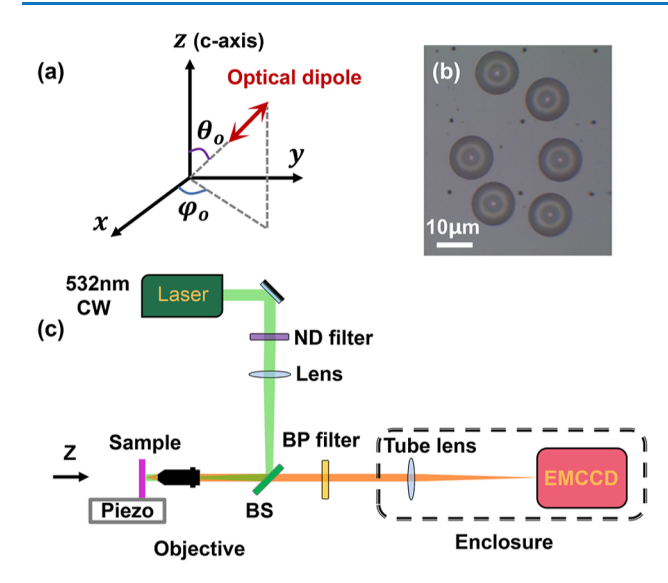


Figure 1. (a) The spatial orientation of a SPE optical dipole moment is specified by the angles φ_o and θ_o . (b) Six fabricated solid immersion lenses (hemispheres of 5 μ m diameter) are shown in the optical microscopic image. (c) Measurement setup for defocused imaging.

In this work, we use the defocused imaging technique to determine the optical dipole orientations of the GaN defect emitters. Our results show that the GaN defect emitters have a single dipole moment (and not an incoherent mixture of more than one dipole moment¹⁵) that is oriented nearly perpendicular to the c-axis. Data collected from many different emitters show that the angular orientation of the dipole moment in the plane perpendicular to the c-axis exhibits a distribution that shows peaks centered at the angles corresponding to the nearest Ga-N bonds and also at the angles corresponding to the nearest Ga-Ga (or N-N) directions. Interestingly, the in-plane angular distribution shows little difference among defect emitters with different emission wavelengths in the 600-700 nm range. Our results are consistent with these emitters being point defects due to substitutional or interstitial impurities (or vacancy-impurity complexes).

RESULTS AND DISCUSSION

The GaN SPEs under investigation were hosted in 4 μ m-thick HVPE-grown semi-insulating GaN epitaxial layers on 430 μ m sapphire substrates. The surface normal direction is the crystal c-axis. The large refractive index contrast between air and GaN reduces, in many different ways, the accuracy with which the orientation of an optical dipole can be determined by using defocused imaging. First, it reduces the photon collection efficiency and the signal-to-noise ratio. Second, it causes optical standing waves to form in the epitaxial layer, making computational determination of the dipole orientation difficult from the recorded data. Finally, the inability to collect photons emitted at large angles from the surface normal direction (as a result of total internal reflection) also degrades the accuracy. To overcome this problem, solid immersion lenses were fabricated around each defect emitter in the form of hemispheres of diameter 5 μ m by focused ion beam milling,⁵ as shown in Figure 1b. An optical microscope setup, shown in Figure 1c, incorporating wide-field laser illumination, was used for pumping the SPEs with a 532 nm wavelength laser. The emitted light was collected using an oil-immersion objective

lens (NA = 1.4), passed through a bandpass filter, and then directed at an EMCCD camera (Andor, Oxford Instruments). The sample was mounted on a piezostage. The objective was used to record the radiation pattern of a SPE by defocusing the objective with respect to the SPE. The defocusing was achieved by moving the piezostage about 1 μ m away from the focal plane of the objective. The EMCCD accumulated 20 frames with an electron multiplying (EM) gain of 500 and had an exposure time of 0.1 s for each frame. A home-built confocal scanning microscope with a Hanbury-Brown and Twiss interferometer was used to measure the emission spectra, polarization patterns, and second-order correlation functions ($g^{(2)}$) of SPEs.⁵

More than a hundred different SPEs were studied in this work. All measurements were carried out at room temperature. Figure 2 shows representative data from five different emitters. Figure 2a—e shows the radiation patterns (defocused images) of emitters E1 through E5 integrated with solid immersion lenses (emitters E2 and E3 belong to the same solid immersion lens). All SPEs exhibit a two-lobe radiation pattern, which, as shown later, is consistent with a single optical dipole oriented almost perpendicular to the crystal c-axis. Figure 2f-j shows the corresponding polarization patterns obtained directly using a polarizer. The polarization data in each case can be fitted with the function $\cos^2(\varphi - \varphi_o)$, consistent with light polarized linearly in a direction φ_{o} that is in agreement with the measured radiation pattern. $\varphi = 0^{\circ}$ corresponds to the direction perpendicular to the wurtzite m-plane. The text in green in Figure 2f-j shows the in-plane angles φ_0 of the dipoles as obtained by fitting polarization patterns with the function $\cos^2(\varphi - \varphi_0)$. Figure 2k-o shows the second-order correlation functions $(g^{(2)})$ measured using the time-tagged time-resolved (TTTR) mode of the correlator (MultiHarp150 from Picoquant) instrument. The small values (below 0.5) of $g^{(2)}(0)$ confirm that all defects are SPEs. The measured emission spectra are plotted in Figure 2p-t. All SPEs exhibit sharp and strong ZPL in the 600-700 nm wavelength range at room temperature. Although the emission wavelengths are different, all emitters in Figure 2 show similar defocused radiation patterns and polarization patterns.

The determination of optical dipole angles θ_o from the defocused images requires analytical or computational modeling. We use the finite-difference time-domain (FDTD) technique to compute the radiation patterns for different dipole angles, θ_o , and compare them with measurements. Figure 3a shows the model structure used in computations. A 4 μ m-thick GaN layer (refractive index n=2.37) is sandwiched between a 430 μ m-thick sapphire substrate (n=1.76) and a 150 μ m-thick immersion oil layer (n=1.51). The solid immersion lens is a hemisphere of diameter 5 μ m. An optical dipole is placed in the center of the solid immersion lens. The angle θ_o of the dipole is varied, and radiation patterns in the far field from the dipole are calculated.

Figure 3b shows the computed far-field radiation patterns for different representative angles $\theta_{\rm o}$ assuming that $\varphi_{\rm o}=0^{\circ}$ and that the dipole emission wavelength is 680 nm. When $\theta_{\rm o}=90^{\circ}$, and the dipole is oriented perpendicular to the c-axis, the radiation pattern has 2-fold rotation symmetry (group $C_{2\nu}$) with respect to the c-axis, with reflection planes at $\varphi=0^{\circ}$ and $\varphi=90^{\circ}$. When $\theta_{\rm o}=0^{\circ}$, and the dipole is oriented along the c-axis, the radiation pattern has complete rotation symmetry (group O(2)). However, the power radiated in the upward direction is extremely small in this case. For all other values of

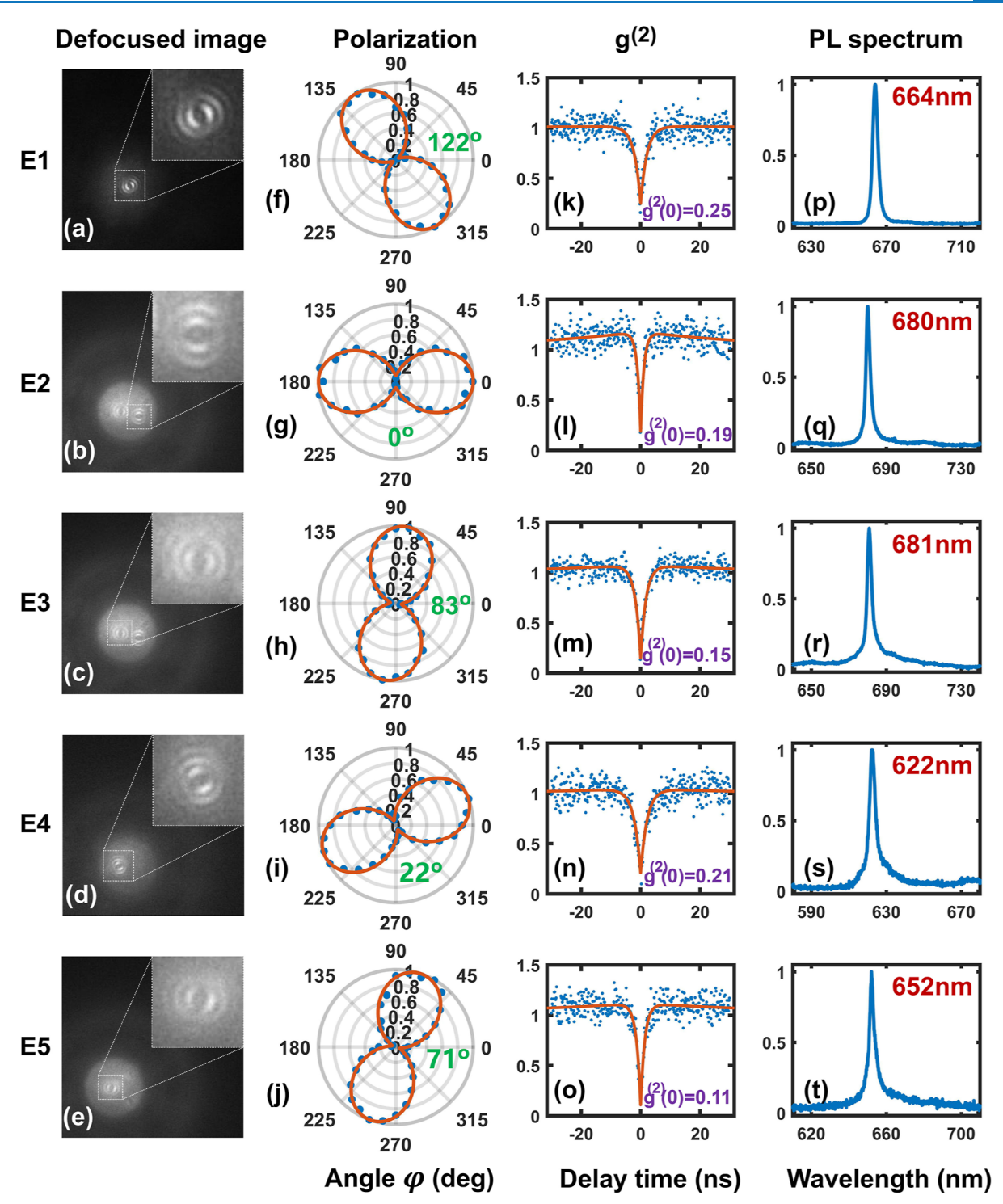


Figure 2. (a–e) Defocused images of light emission from five different SPEs, E1–E5, integrated with solid immersion lenses are shown. Insets show the zoomed-in radiation patterns of each SPE. (f-j) Measured polarization patterns of the emitted light are plotted as a function of the inplane angle φ . $\varphi = 0^{\circ}$ corresponds to the direction perpendicular to the wurtzite m-plane. The text in green shows the in-plane angles φ_o of the dipoles as obtained by fitting data with the function $\cos^2(\varphi - \varphi_o)$. (k–o) Measured second-order correlation functions are plotted. (p–t) Measured photoluminescence (PL) spectra are plotted. All measurements were performed at room temperature.

 $\theta_{\rm o}$, the radiation pattern has lower symmetry (group $C_{1\nu}$) with a single reflection plane at $\varphi=0^{\circ}$. As shown in Figure 3b, the lowering of symmetry in the radiation pattern from $C_{2\nu}$ to $C_{1\nu}$ as the dipole angle is reduced from $\theta_{\rm o}=90^{\circ}$, makes the pattern more asymmetric with respect to the $\varphi=90^{\circ}$ plane. The accuracy with which the dipole angle $\theta_{\rm o}$ can be determined from the measured radiation pattern depends on the exact and

detailed comparison between data and theory and also on the signal-to-noise ratio in the measured data. As shown in Figure 2a-e, the measured radiation patterns of all SPEs have approximately 2-fold $C_{2\nu}$ symmetry, which implies that all SPEs are oriented perpendicular (or almost perpendicular) to the c-axis (i.e., $\theta_{\rm o} = 90^{\circ}$). However, noise in our measurements can be used to put an error margin on the value of $\theta_{\rm o}$. By

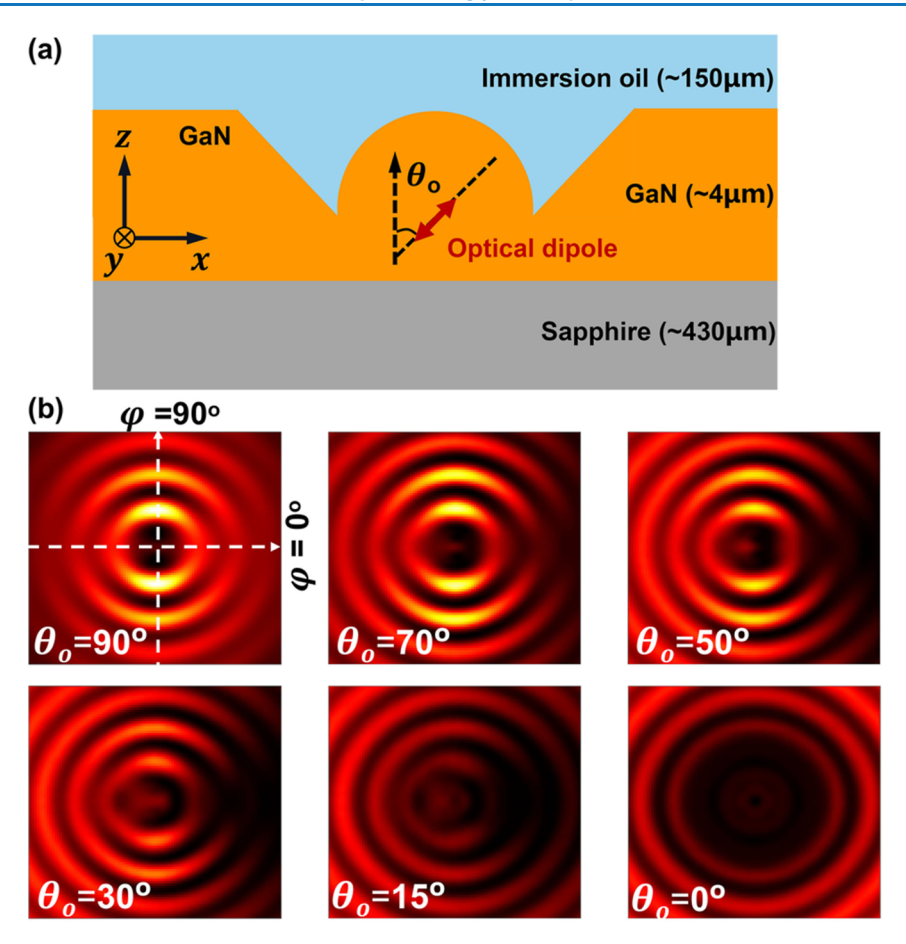


Figure 3. (a) Structure used in numerical (FDTD) computations. The 4 μ m GaN layer is sandwiched by an oil immersion layer and a sapphire substrate. The diameter of the solid immersion lens is 5 μ m. (b) The calculated far-field radiation patterns from the dipole are plotted for different dipole out-of-plane angles θ_o . The radiation pattern has $C_{2\nu}$ symmetry for $\theta_o = 90^\circ$, O(2) symmetry for $\theta_o = 0^\circ$, and $C_{1\nu}$ symmetry for all angles in between. Since the radiated power in the vertical direction is also a function of the dipole angle, the contrast is adjusted in the figures shown for better visibility as follows: ($\theta_o = 90^\circ$, contrast 1×), (70° , 1×), (50° , 2×), (30° , 3×), (15° , 5×), and (0° , 10×).

comparing the measurements with the computed images and taking into account the noise in our data, we estimate that $\theta_{\rm o}$ for all SPEs satisfies $70^{\circ} < \theta_{\rm o} < 110^{\circ}$ irrespective of the wavelength and the in-plane orientation of the SPE dipole. This range specifies the noise-limited error margin in our determination of $\theta_{\rm o}$.

Other factors that can affect the determination of the dipole angle θ_0 include the following: (i) the emission wavelength of a SPE can be different from 680 nm, the wavelength used in our computations, and (ii) in actual samples, SPEs are not exactly located at the location assumed in the computations (see Figure 3a). Points whose distance r from a dipole satisfies $r \gg$ $\lambda/(2\pi n) \approx 50$ nm, where n is the refractive index of GaN, constitute the radiation far-field region. If a dipole is away from all interfaces by at least 1 μ m (~20 times $\lambda/(2\pi n)$), and the lens structure does not favor the formation of strong standing waves, one can expect that the recorded radiation pattern will not get much affected by the exact location of the dipole inside the lens. The SPEs studied in this work were selected such that they were at least a micrometer away from the top and bottom interfaces of the GaN epitaxial layer to avoid surface contamination and interface defects. Furthermore, the offsets between the centers of the solid immersion lenses and the SPEs due to fabrication errors were generally less than 1 μ m. This ensured that all interfaces were in the far-field regions of the SPEs. Numerical computations indeed show that when the

above conditions are fulfilled, the effect of the location of the dipole on the radiation pattern and on the accuracy with which $\theta_{\rm o}$ can be determined is small enough to be almost negligible compared to the accuracy limitation imposed by the presence of noise, as discussed above. This can be seen in our experimental data as well (Figure 2a–e) where the approximate $C_{2\nu}$ symmetry is seen for all SPEs irrespective of their exact location within the lens. Similarly, numerical computations show that the effect of variation in the emission wavelength of a SPE in the 600–700 nm range on the radiation pattern is small enough to be ignored.

Finally, we investigate the distribution of the in-plane angle φ_o of the SPEs and examine if any correlations exist between these angles and the underlying crystal structure. Since the wurtzite crystal structure has an in-plane 3-fold rotation symmetry and the linearly polarized light from the SPEs has a 2-fold symmetry, we classify all measured SPEs according to the angle mod $(\varphi_o, 60^\circ)$. The resulting distribution is plotted in Figure 4a for close to 100 emitters with different emission wavelengths in the 600–700 nm range. The four wavelengths shown are the center wavelengths of the bins in which SPEs with emission wavelengths close to the bin center wavelength (within ± 5 nm) were placed in making the plot. Several interesting features are visible in this plot. First, SPEs of all wavelengths exhibit very similar angular distributions. Second, the angular distributions are fairly wide. Third, the angular

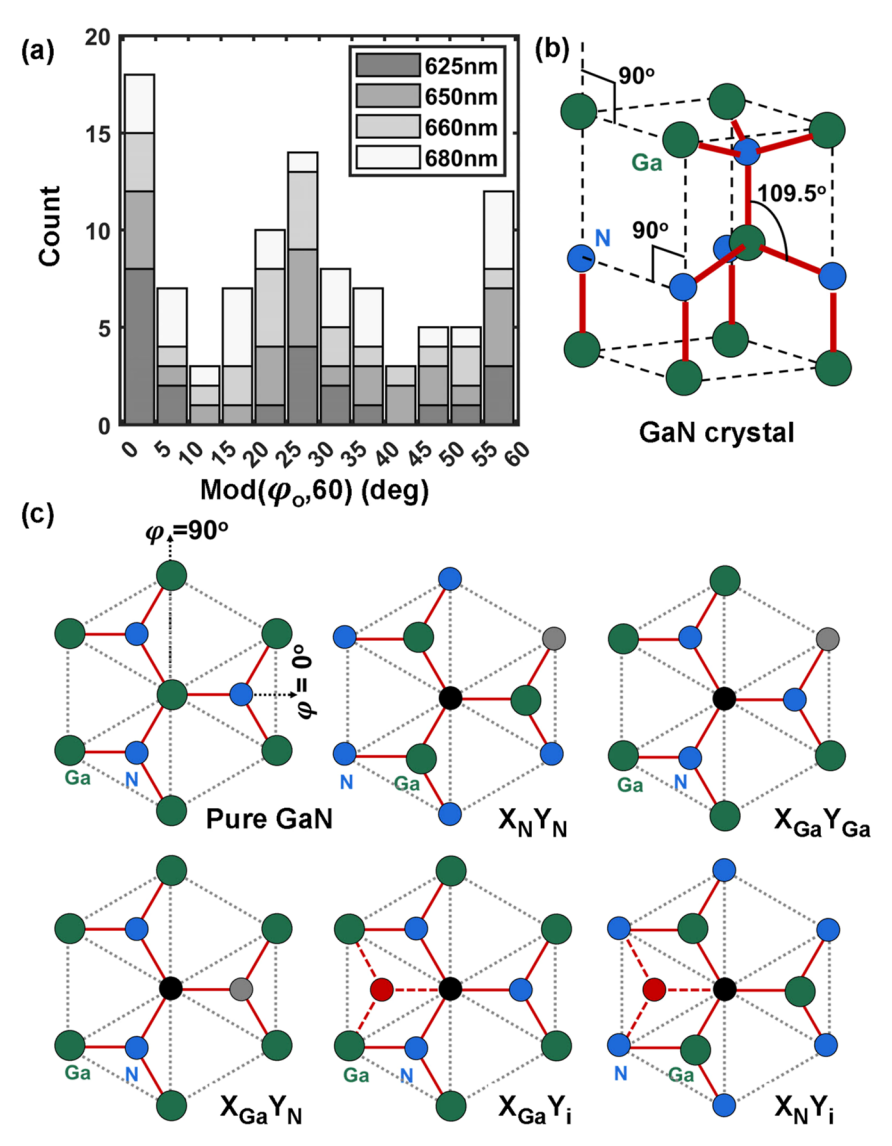


Figure 4. (a) The distributions of in-plane optical dipole angles mod $(\varphi_o, 60^\circ)$ for different wavelength SPEs are shown. (b) GaN wurtzite crystal structure (side view). (c) Impurity/vacancy complexes of the forms $X_N Y_{Ni}, X_{Ga} Y_{Ga}, X_{Ga} Y_{Ni}, X_{Ga} Y_{i}$, and $X_N Y_i$ are depicted. X and Y stand for an impurity atom or a vacancy (if on a lattice site), and the subscript i stands for an interstitial (shown in red). Substitutional impurities and vacancies are shown in black or gray. The leftmost figure in the top row shows a pure GaN crystal (top view).

distributions show two distinct peaks at angles close to 0° (or 60°) and 30° . These angles correspond to the directions between the nearest Ga–N bonds and the nearest Ga–Ga (or N–N) directions in the wurtzite crystal structure of GaN, as depicted in the first subfigure in Figure 4c.

The information obtained via defocused imaging about the optical dipole orientation of GaN SPEs in the 600–700 nm wavelength range can help identify the nature and origin of the SPEs. First, a single substitutional impurity or a vacancy at either the Ga or N site is expected to have $C_{3\nu}$ point group symmetry with the c-axis as the 3-fold axis of rotation. The $C_{3\nu}$ group has two one-dimensional representations, A_1 and A_2 , and one two-dimensional representation, E. Optical transitions are allowed between states with the same A_1 , A_2 , or E symmetry and between states with A_1 or A_2 symmetry and E symmetry. In all of these cases, linearly polarized light emission with a single optical dipole axis, as observed in our measurements, is not possible (unless the double degeneracy between the states with E symmetry is somehow lifted). Next, we consider impurity/vacancy complexes of the forms $X_N Y_N$, $X_{Ga} Y_{Ga}$

 $X_{Ga}Y_{N}$, $X_{Ga}Y_{i}$, and $X_{N}Y_{i}$ (see Figure 4c). X and Y stand for an impurity/substitutional atom or a vacancy (if on a lattice site), and the subscript i stands for an interstitial. If one assumes that the optical dipole moment is along the axis of the X-Y complex, then this family of defects could explain the measured dipole orientations (angles $\theta_{\rm o}$ and $\varphi_{\rm o}$) of the SPEs (note the 109.5 and 90 $^{\circ}$ angles between the c-axis and the nearest Ga-N bonds and the nearest Ga-Ga (or N-N) directions, respectively, in Figure 4b). Several first-principles studies have been reported for point defects in GaN. Point defects in which one of *X* and *Y* is carbon or iron and the other is carbon, hydrogen, oxygen, or a vacancy are promising candidates as computations have shown these point defects to have relatively small formation energies and their computed ZPL photon emission energies are in the neighborhood of the observed emission energies. 19-23 However, computed optical dipole orientations have not been reported in the literature for all of these defects. In the case when both X and Y are carbon atoms, the optical dipoles are known to be oriented along the X-Y axis. ¹⁹ The experimentally observed departure from exact

0 and 30° values of mod (φ_0 , 60°) could be due to the fact that the presence of impurity atoms causes lattice distortion, and therefore, the actual positions of the atoms are not expected to be as shown in Figure 4c. 19,20,23 Supporting evidence for these defects also comes from secondary ion mass spectrometry (SIMS) data. The semi-insulating GaN samples used in this work were iron-doped, and the iron concentration measured by SIMS was $\sim 7 \times 10^{17}/\text{cm}^3$. SIMS also showed carbon, hydrogen, and oxygen concentrations of $\sim 5 \times 10^{16}/\text{cm}^3$, $\sim 3 \times 10^{16}/\text{cm}^3$ 10^{17} /cm³, and $\sim 10^{16}$ /cm³, respectively. Whereas the defects mentioned above are all extrinsic, recently an intrinsic antisitevacancy complex $N_{Ga}V_N$ (also of the type $X_{Ga}Y_N$) has also been suggested as a possible candidate for SPEs with emission wavelengths close to 625 nm.²⁴ As a final word, we note here that the SPE density in our samples is less than $10^{10}/{\rm cm}^3$. This means that impurity atoms in concentrations much lower than the SIMS detection limit could also underlie the observed SPEs in our samples.

CONCLUSIONS

In conclusion, we used the defocused imaging technique to study the optical dipole structures and orientations of defect SPEs in GaN. Our experimental results, backed up by FDTD calculations, show that GaN defect SPEs in the 600–700 nm wavelength range consist of a single optical dipole, and the dipole orientation is approximately perpendicular to the crystal c-axis. The angular orientation of the dipole moment in the plane perpendicular to the c-axis exhibits a distribution that shows peaks centered at the angles corresponding to the nearest Ga—N bonds and also at the angles corresponding to the nearest Ga—Ga (or N—N) directions. Our findings are consistent with these SPEs being point defects. We hope that this work will stimulate further theoretical and experimental studies of the nature and origin of GaN SPEs.

ASSOCIATED CONTENT

Supporting Information

The Supporting Information is available free of charge at https://pubs.acs.org/doi/10.1021/acsphotonics.3c00917.

Sample fabrication section, precise location of defect emitters acquired by a spatial PL map, and a representative SEM image of fabricated solid immersion lenses; home-built confocal scanning microscope setup used for the measurement of PL spectra, polarization patterns, and second-order correlation functions of defect emitters; error margin in the estimation of the angle $\theta_{\rm o}$ of optical dipoles; and emission patterns as a function of the defocus depth (PDF)

AUTHOR INFORMATION

Corresponding Author

Yifei Geng — School of Electrical and Computer Engineering, Cornell University, Ithaca, New York 14853, United States; orcid.org/0000-0001-8438-3384; Email: yg474@ cornell.edu

Authors

Debdeep Jena — School of Electrical and Computer Engineering, Cornell University, Ithaca, New York 14853, United States; Department of Materials Science and Engineering, Cornell University, Ithaca, New York 14853, United States Gregory D. Fuchs — School of Applied and Engineering Physics, Cornell University, Ithaca, New York 14853, United States; occid.org/0000-0003-4343-8523

Warren R. Zipfel – Meinig School of Biomedical Engineering, Cornell University, Ithaca, New York 14853, United States Farhan Rana – School of Electrical and Computer Engineering, Cornell University, Ithaca, New York 14853, United States

Complete contact information is available at: https://pubs.acs.org/10.1021/acsphotonics.3c00917

Funding

NSF MRSEC program (DMR-1719875) and NSF-RAISE:-TAQS (ECCS-1838976).

Notes

The authors declare no competing financial interest.

ACKNOWLEDGMENTS

The authors thank Len van Deurzen for SIMS information on the sample. This work was supported by the Cornell Center for Materials Research with funding from the NSF MRSEC program (DMR-1719875) and also by the NSF-RAISE:TAQS (ECCS-1838976).

REFERENCES

- (1) Aharonovich, I.; Englund, D.; Toth, M. Solid-state single-photon emitters. *Nat. Photonics* **2016**, *10*, 631–641.
- (2) Berhane, A. M.; Jeong, K.-Y.; Bodrog, Z.; Fiedler, S.; Schröder, T.; Triviño, N. V.; Palacios, T.; Gali, A.; Toth, M.; Englund, D.; Aharonovich, I. Bright Room-Temperature Single-Photon Emission from Defects in Gallium Nitride. *Adv. Mater.* 2017, 29, 1605092.
- (3) Berhane, A. M.; Jeong, K.-Y.; Bradac, C.; Walsh, M.; Englund, D.; Toth, M.; Aharonovich, I. Photophysics of GaN single-photon emitters in the visible spectral range. *Phys. Rev. B* **2018**, *97*, 165202.
- (4) Luo, J.; Geng, Y.; Rana, F.; Fuchs, G. Room-Temperature Optically Detected Magnetic Resonance of GaN Defect Single-Photon Emitters. *CLEO* 2023; Optica Publishing Group, 2023.
- (5) Geng, Y.; Luo, J.; van Deurzen, L.; Xing, H.; Jena, D.; Fuchs, G. D.; Rana, F. Dephasing by optical phonons in GaN defect single-photon emitters. *Sci. Rep.* **2023**, *13*, 8678.
- (6) Zhou, J.-Y.; Li, Q.; Hao, Z.-Y.; Yan, F.-F.; Yang, M.; Wang, J.-F.; Lin, W.-X.; Liu, Z.-H.; Liu, W.; Li, H.; You, L.; Xu, J.-S.; Li, C.-F.; Guo, G.-C. Experimental determination of the dipole orientation of single color centers in silicon carbide. *ACS Photonics* **2021**, *8*, 2384–2391.
- (7) Chen, G.; Liu, Y.; Song, M.; Wu, B.; Wu, E.; Zeng, H. Photoluminescence Enhancement Dependent on the Orientations of Single NV Centers in Nanodiamonds on a Gold Film. *IEEE J. Sel. Top. Quantum Electron.* **2013**, *19*, 4602404.
- (8) Dolan, P. R.; Li, X.; Storteboom, J.; Gu, M. Complete determination of the orientation of NV centers with radially polarized beams. *Opt. Express* **2014**, *22*, 4379–4387.
- (9) Lieb, M. A.; Zavislan, J. M.; Novotny, L. Single-molecule orientations determined by direct emission pattern imaging. *J. Opt. Soc. Am. B* **2004**, *21*, 1210–1215.
- (10) Jasny, J.; Sepioł, J. Single molecules observed by immersion mirror objective. A novel method of finding the orientation of a radiating dipole. *Chem. Phys. Lett.* **1997**, 273, 439–443.
- (11) Böhmer, M.; Enderlein, J. Orientation imaging of single molecules by wide-field epifluorescence microscopy. *J. Opt. Soc. Am. B* **2003**, *20*, 554–559.
- (12) Patra, D.; Gregor, I.; Enderlein, J. Image analysis of defocused single-molecule images for three-dimensional molecule orientation studies. *J. Phys. Chem. A* **2004**, *108*, 6836–6841.
- (13) Gardini, L.; Capitanio, M.; Pavone, F. S. 3D tracking of single nanoparticles and quantum dots in living cells by out-of-focus imaging with diffraction pattern recognition. *Sci. Rep.* **2015**, *5*, 16088–16110.

- (14) Schuster, R.; Barth, M.; Gruber, A.; Cichos, F. Defocused wide field fluorescence imaging of single CdSe/ZnS quantum dots. *Chem. Phys. Lett.* **2005**, *413*, 280–283.
- (15) Patra, D.; Gregor, I.; Enderlein, J.; Sauer, M. Defocused imaging of quantum-dot angular distribution of radiation. *Appl. Phys. Lett.* **2005**, *87*, 101103.
- (16) Lethiec, C.; Pisanello, F.; Carbone, L.; Bramati, A.; Coolen, L.; Maitre, A. Polarimetry-based analysis of dipolar transitions of single colloidal CdSe/CdS dot-in-rods. *New J. Phys.* **2014**, *16*, 093014.
- (17) Habuchi, S.; Oba, T.; Vacha, M. Multi-beam single-molecule defocused fluorescence imaging reveals local anisotropic nature of polymer thin films. *Phys. Chem. Chem. Phys.* **2011**, *13*, 7001–7007.
- (18) Su, L.; Yuan, H.; Lu, G.; Rocha, S.; Orrit, M.; Hofkens, J.; Uji-i, H. Super-resolution localization and defocused fluorescence microscopy on resonantly coupled single-molecule, single-nanorod hybrids. *ACS Nano* **2016**, *10*, 2455–2466.
- (19) Matsubara, M.; Bellotti, E. A first-principles study of carbonrelated energy levels in GaN. I. Complexes formed by substitutional/ interstitial carbons and gallium/nitrogen vacancies. *J. Appl. Phys.* **2017**, *121*, 195701.
- (20) Matsubara, M.; Bellotti, E. A first-principles study of carbon-related energy levels in GaN. II. Complexes formed by carbon and hydrogen, silicon or oxygen. *J. Appl. Phys.* **2017**, *121*, 195702.
- (21) Wickramaratne, D.; Shen, J.-X.; Dreyer, C. E.; Alkauskas, A.; Van de Walle, C. G. Electrical and optical properties of iron in GaN, AlN, and InN. *Phys. Rev. B* **2019**, *99*, 205202.
- (22) Lyons, J. L.; Wickramaratne, D.; Van de Walle, C. G. A first-principles understanding of point defects and impurities in GaN. *J. Appl. Phys.* **2021**, *129*, 111101.
- (23) Lyons, J. L.; Glaser, E. R.; Zvanut, M. E.; Paudel, S.; Iwinska, M.; Sochacki, T.; Bockowski, M. Carbon complexes in highly C-doped GaN. *Phys. Rev. B* **2021**, *104*, 075201.
- (24) Yuan, J.; Hou, Y.; Yang, Z.; Chen, F.; Li, Q. GaN as a Material Platform for Single-Photon Emitters: Insights from Ab Initio Study. *Adv. Opt. Mater.* **2023**, *11*, 2202158.